

SIMULATIONS ON A MOVING MESH:
THE CLUSTERED FORMATION OF POPULATION III PROTOSTARS

THOMAS H. GREIF¹, VOLKER SPRINGEL^{2,3}, SIMON D. M. WHITE¹, SIMON C. O. GLOVER⁴, PAUL C. CLARK⁴,
ROWAN J. SMITH⁴, RALF S. KLESSEN⁴ & VOLKER BROMM⁵

Draft version June 2, 2019

ABSTRACT

The cosmic dark ages ended a few hundred million years after the Big Bang, when the first stars began to fill the universe with new light. It has generally been argued that these stars formed in isolation and were extremely massive – perhaps 100 times as massive as the Sun. We here use a series of high-resolution hydrodynamical simulations performed with the moving mesh code AREPO to show that this view may require revision. We follow the collapse of five independent minihalos from cosmological initial conditions, through the runaway condensation of their central gas clouds, to the formation of the first protostar, and beyond for a further 1000 years. During this latter accretion phase, we represent the optically thick regions of protostars by sink particles. Gas accumulates rapidly in the circumstellar disk around the first protostar, fragmenting vigorously to produce a small group of protostars. After an initial burst, gravitational instability recurs periodically, forming additional protostars with masses ranging from ~ 0.1 to $10 M_{\odot}$. Although the shape, multiplicity, and normalization of the protostellar mass function depend on the details of the sink-particle algorithm, fragmentation into protostars with diverse masses occurs in all cases, with low-mass objects occasionally being ejected through gravitational slingshot effects. Depending on the efficiency of later accretion and merging, Population III stars may enter the main sequence in clusters and with much more diverse masses than is commonly assumed. A few may even survive to the present day.

Subject headings: cosmology: theory — early universe — hydrodynamics — methods: numerical — stars: formation

1. INTRODUCTION

Over the past decade, a consensus has emerged on how the first, so-called Population III (Pop III), stars may have formed out of the hydrogen and helium forged in the Big Bang (Barkana & Loeb 2001; Bromm & Larson 2004; Bromm et al. 2009). Non-linear structure formation from an initially nearly featureless universe began when dark matter minihalos with masses of order $10^6 M_{\odot}$ collapsed at redshifts $z \sim 20 - 50$, confining gas within their gravitational potential wells (Haiman et al. 1996; Tegmark et al. 1997). Cooling through ro-vibrational transitions of newly formed molecular hydrogen then triggered runaway collapse at the center of the halo, resulting in the formation of a protostar with density more than twenty orders of magnitude higher than the cosmic mean (Yoshida et al. 2008). The envelope of the accreting protostar remained hot due to the lack of cooling by metals and dust, so that accretion rates were on average higher than in star-formation regions today (Mac Low & Klessen 2004; McKee & Ostriker 2007; Zinnecker & Yorke 2007). With a few exceptions (Turk et al. 2009), simulations of this initial collapse

phase have shown no fragmentation (Abel et al. 2002; Bromm et al. 2002; Bromm & Loeb 2004; Yoshida et al. 2006; O’Shea & Norman 2007; Yoshida et al. 2008), leading to the conclusion that the first stars formed in isolation and were extremely massive.

In contrast, studies of present-day star formation have generally found fragmentation to occur shortly after the formation of the first protostar (Klessen & Burkert 2000; Bate et al. 2003; Krumholz et al. 2009; Peters et al. 2010). Although simulations with idealized initial conditions have suggested that the same could hold for metal-poor gas in the early universe (Clark et al. 2008), simulations of primordial star formation with the resolution to see individual protostars have not yet probed the relevant regime because of the extremely small timesteps required near the stellar surface (Yoshida et al. 2008). Here we achieve this goal by using a new hydrodynamics technique coupled to a sink-particle algorithm similar to those often used in studies of present-day star formation (Bate et al. 1995; Krumholz et al. 2004; Jappsen et al. 2005; Federrath et al. 2010).

A first study of fragmentation of primordial gas in minihalos using the sink particle approach has been reported by Stacy et al. (2010b). In a complementary effort, Clark et al. (2011) investigated the fragmentation of isolated metal-free gas clouds with different degrees of turbulence. Both studies found a disk to form around the first protostar and thereafter to fragment into a small cluster. These results challenged the idea that Pop III stars formed in isolation, but their significance was uncertain since they either employed idealized initial conditions or inserted sink particles at densities far below those of protostars, so that their immediate vicinity was

¹Max-Planck-Institut für Astrophysik, Karl-Schwarzschild-Straße 1, 85740 Garching bei München, Germany

²Heidelberg Institute for Theoretical Studies, Schloss-Wolfsbrunnengasse 35, 69118 Heidelberg, Germany

³Zentrum für Astronomie der Universität Heidelberg, Astronomisches Recheninstitut, Mönchhofstr. 12-14, 69120 Heidelberg, Germany

⁴Zentrum für Astronomie der Universität Heidelberg, Institut für Theoretische Astrophysik, Albert-Ueberle-Straße 2, 69120 Heidelberg, Germany

⁵Department of Astronomy and Texas Cosmology Center, University of Texas, Austin, TX 78712, USA

Table 1
Simulation parameters

Simulation	Size [kpc]	Particles	$M_{\text{dm}} [M_{\odot}]$	$M_{\text{gas}} [M_{\odot}]$	σ_8	$M_{\text{vir}} [M_{\odot}]$	$r_{\text{vir}} [\text{pc}]$	λ	z_{coll}
MH-1	1000	512^3	4.25	0.72	0.81	5.8×10^5	150	0.059	18.6
MH-2	500	256^3	4.25	0.72	0.9	3.0×10^5	110	0.055	19.5
MH-3	250	128^3	4.25	0.72	1.2	2.3×10^5	94	0.073	20.9
MH-4	500	256^3	4.25	0.72	1.1	3.1×10^5	97	0.044	22.6
MH-5	500	256^3	4.25	0.72	1.3	1.8×10^5	58	0.038	31.7

The comoving box sizes, particle numbers, initial DM and gas particle masses, and normalizations used in the simulations, as well as the virial masses, virial radii, spin parameters, and collapse redshifts of the first minihalos that form. The halo properties agree well with previous grid-based studies (e.g. Machacek et al. 2001; O’Shea & Norman 2007), while the halo masses are typically lower than in SPH simulations (Yoshida et al. 2003).

not resolved. Furthermore, computing time constraints limited the simulation presented in Stacy et al. (2010b) to a single realization of the star-formation environment, so that the frequency of fragmentation in minihalos could not be addressed.

We here report on a series of hydrodynamical simulations performed with the quasi-Lagrangian moving mesh code AREPO (Springel 2010a). Its high accuracy, flexibility, and efficiency allow us to follow the evolution of the gas in five statistically independent minihalos from fully cosmological initial conditions down to the optically thick regime where primordial protostars are born. We also use a sink-particle approach to capture the subsequent accretion phase, which allows us to reach well beyond the formation of the first protostar, and circumvent the limitations posed in previous high-resolution *ab initio* calculations of primordial star formation (Yoshida et al. 2008). The five realizations give us an indication of how common fragmentation is, and of the shape of the mass function of Pop III protostars during the early stages of accretion.

The structure of our work is as follows: In Section 2, we describe the numerical setup and physical ingredients of the simulations. In Section 3, we present the results of the simulations and a discussion of radiation feedback, followed by an investigation of the caveats of the sink particle treatment. Finally, in Section 4 we summarize and draw conclusions. All distances quoted in this paper are in proper units, unless noted otherwise.

2. NUMERICAL METHODOLOGY

We here provide details about the set-up of our dark matter (DM) simulations, the employed resimulation technique, and the main simulation runs with the hydrodynamic moving mesh code AREPO. We also discuss the implementation of the on-the-fly mesh refinement technique, the sink-particle treatment, and the chemistry and cooling model.

2.1. Dark Matter Simulations

Our DM simulations are initialized in cosmological boxes with 250, 500 and 1000 kpc (comoving) on a side, using 128^3 , 256^3 and 512^3 particles of mass $272 M_{\odot}$, so that minihalos with a characteristic mass of $5 \times 10^5 M_{\odot}$ are resolved by $\simeq 2 \times 10^3$ particles and a comoving gravitational softening length of 68 pc. We use an initial fluctuation power spectrum for a Λ cold dark matter (Λ CDM) cosmology at a starting redshift of $z = 99$, with matter density $\Omega_m = 1 - \Omega_{\Lambda} = 0.27$, baryon density $\Omega_b =$

0.046, Hubble parameter $h = H_0/100 \text{ km s}^{-1} \text{ Mpc}^{-1} = 0.71$ (where H_0 is the present Hubble expansion rate), spectral index $n_s = 0.96$, and a linearly extrapolated present-day normalization of $\sigma_8 = 0.81$. These parameters are based on the five-year WMAP results (Komatsu et al. 2009). In a number of cases, we slightly increase the normalization to mimic rare overdense regions of the universe that can not be captured with the limited box sizes used here.

All our DM simulations were evolved with the TreePM/SPH code GADGET-3 (last described in Springel 2005) until the first minihalo with a virial mass exceeding $5 \times 10^5 M_{\odot}$ collapses, thereby providing a target region for our subsequent resimulations. In this study, we restrict ourselves to the analysis of five independent realizations of the minihalos identified in the large-scale DM runs, denoted MH-1 to MH-5. The most important parameters and properties of the minihalos are summarized in Table 1.

2.2. Resimulation Technique

Once the location of a minihalo in our parent simulation has been determined, we construct a high-resolution study of this object by first identifying all particles within the virial radius and a sufficiently large boundary region around it. These particles are then traced back to their initial conditions, yielding the Lagrangian region that formed the object. To construct new initial conditions, each particle in this region is replaced by 64 DM particles and 64 mesh-generating points which produce the space-filling cells that are used for our hydrodynamic calculations.

Cells and DM particles outside of the high-resolution region are replaced by ever higher mass particles with increasing distance from the target halo, such that the resolution coarsens significantly far away from the target halo, yet the gravitational tidal field that influences its formation is still followed with high accuracy. This step reduces the total number of particles and cells in the refined initial conditions to $\simeq 2 \times 10^6$. The simulation box is then centered on the target halo and reinitialized at $z = 99$ based on the original realization of the density field, but augmented with additional small-scale power in the high-resolution region that can now be represented. The initial DM particle and cell masses in the high-resolution region (before any further run-time refinement) are given by $\simeq 4.25 M_{\odot}$ and $\simeq 0.72 M_{\odot}$, respectively, and the comoving gravitational softening length of the refined DM component is set to 17 pc.

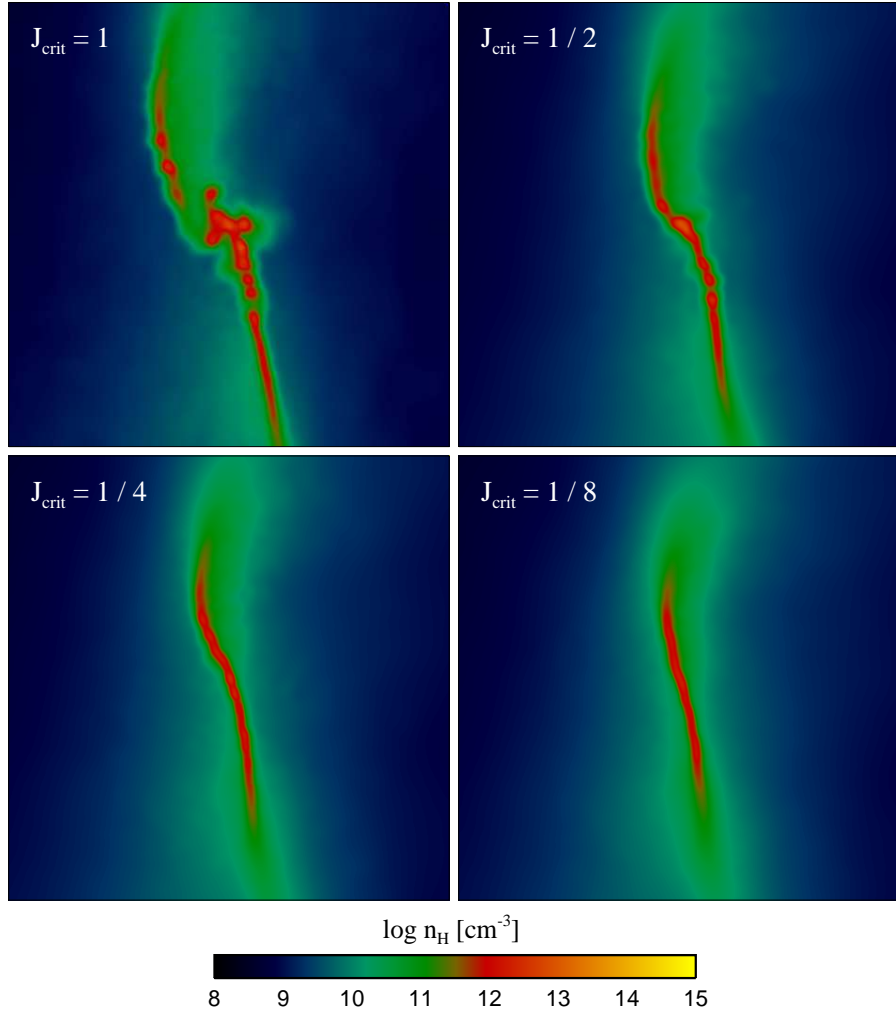


Figure 1. A test of the classical Truelove et al. (1998) criterion in AREPO with the Boss & Bodenheimer (1979) setup in the formulation of Burkert & Bodenheimer (1993). The individual panels compare simulations with on-the-fly mesh refinement using critical Jeans numbers of 1, 1/2, 1/4, and 1/8, respectively, and show the density-squared weighted hydrogen density projected along the line of sight in a box with 200 AU on a side, centered on one of the two main clumps. The amount of artificial fragmentation increases dramatically once the local Jeans length is resolved by less than four cells. The resolution required in AREPO is therefore very similar to the requirement of AMR codes.

2.3. The Moving Mesh Code AREPO

We follow the collapse of the gas in the refined mini-halos with the cosmological moving mesh code AREPO (Springel 2010a). AREPO is a second-order accurate finite volume method that solves the Euler equations based on a piece-wise linear reconstruction and the calculation of hydrodynamical fluxes at every cell face with an exact Riemann solver. The principal difference of AREPO compared to Eulerian mesh codes is that its computational mesh is constructed as the Voronoi tessellation of a set of mesh-generating points. These points can be moved with the flow velocity itself, making the mesh automatically adaptive in a Lagrangian fashion. This technique greatly reduces the numerical diffusivity of mesh-based hydrodynamics, especially when large bulk flows are present. In fact, the results of the code become Galilean-invariant, unlike those of ordinary Eulerian mesh codes. In addition, the unstructured Voronoi mesh of AREPO avoids the introduction of preferred directions, which are present in Cartesian meshes.

The novel AREPO scheme hence combines the accuracy of mesh-based hydrodynamics with the natural adaptivity and translational invariance usually only provided by the smoothed particle hydrodynamics (SPH) technique. In terms of hydrodynamical accuracy, the grid-based approach of AREPO alleviates a number of shortcomings encountered with SPH (Monaghan 2005). Among these are the inherent noise of the kernel estimates, the artificial viscosity, and the slow convergence rate of SPH in three dimensions (Springel 2010b). Further important improvements of AREPO lie in the more accurate treatment of shocks and turbulence, and of fluid instabilities (Agertz et al. 2007). Compared to adaptive mesh refinement (AMR) codes, a significant advantage of AREPO lies in its ability to continuously adjust its resolution when density fluctuations grow under self-gravity. This key feature of Lagrangian codes is ideal for gravitational collapse problems. If the bulk velocities are large, AREPO can use larger timesteps than AMR codes and exhibits lower numerical diffusion errors at comparable spatial resolution.

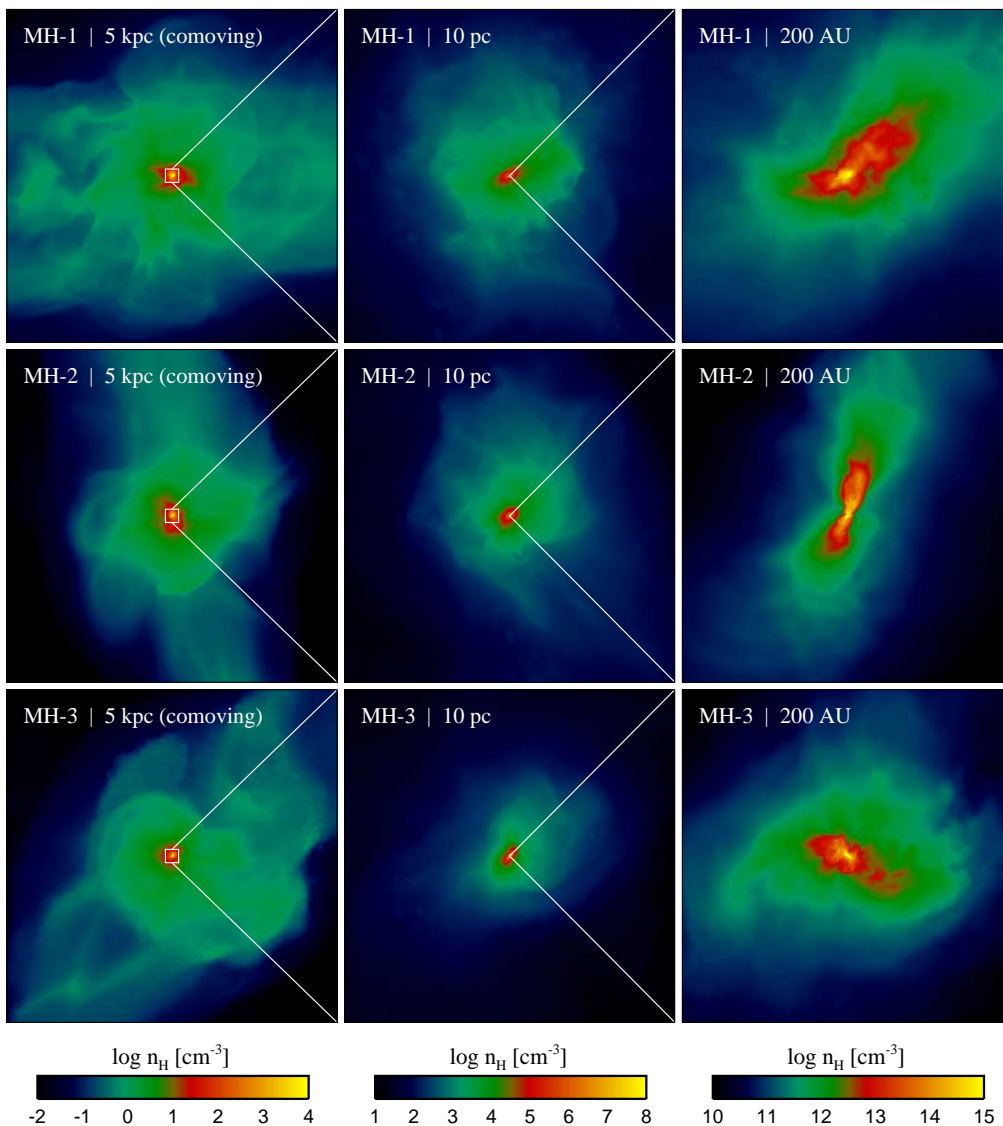


Figure 2. A sequential zoom-in on the gas in each minihalo. Shown is the density-squared weighted hydrogen density projected along the line of sight. The gas virializes on a scale of 5 kpc (comoving), followed by the runaway collapse of the central 10 pc, where the gas becomes self-gravitating and decouples from the dark matter. In the final stages of the collapse, a fully molecular core forms on a scale of 200 AU. The visible turbulence induced by the virialization of the dark matter halo survives down to the smallest scales and later influences the fragmentation of the gas.

We note that the computational speed of AREPO in simulations of cosmic structure formation is roughly on par with GADGET-3 for an equal number of hydrodynamic resolution elements, despite its comparatively complex mesh-construction calculations. This is in part due to the large cost of accurate calculations of self-gravity, which dominate over the hydrodynamics both in AREPO and GADGET-3. Both codes compute the gravitational field with a fully adaptive combination of a particle-mesh (PM) solver for large-scale forces, and a hierarchical multipole expansion for short-range forces. In any case, because of the higher accuracy of AREPO compared to SPH for an equal number of resolution elements, this means that AREPO is the more efficient method. The faster convergence rate of AREPO also implies that

its accuracy advantage increases further if more resolution elements are employed.

The mesh-generating points of AREPO can still be interpreted as Lagrangian fluid particles, if desired, which greatly simplifies the (re)use of well-tested techniques from SPH codes, such as implementations of gas chemistry or sink particles, an approach we employ extensively in this study. Also, even though AREPO's fluid cells follow the motion of the gas and hence maintain a roughly constant gas mass, it is sometimes necessary to refine the mass resolution per cell during a calculation. This can be done accurately in the mesh-based approach of AREPO, as we discuss next.

2.4. Mesh Refinement

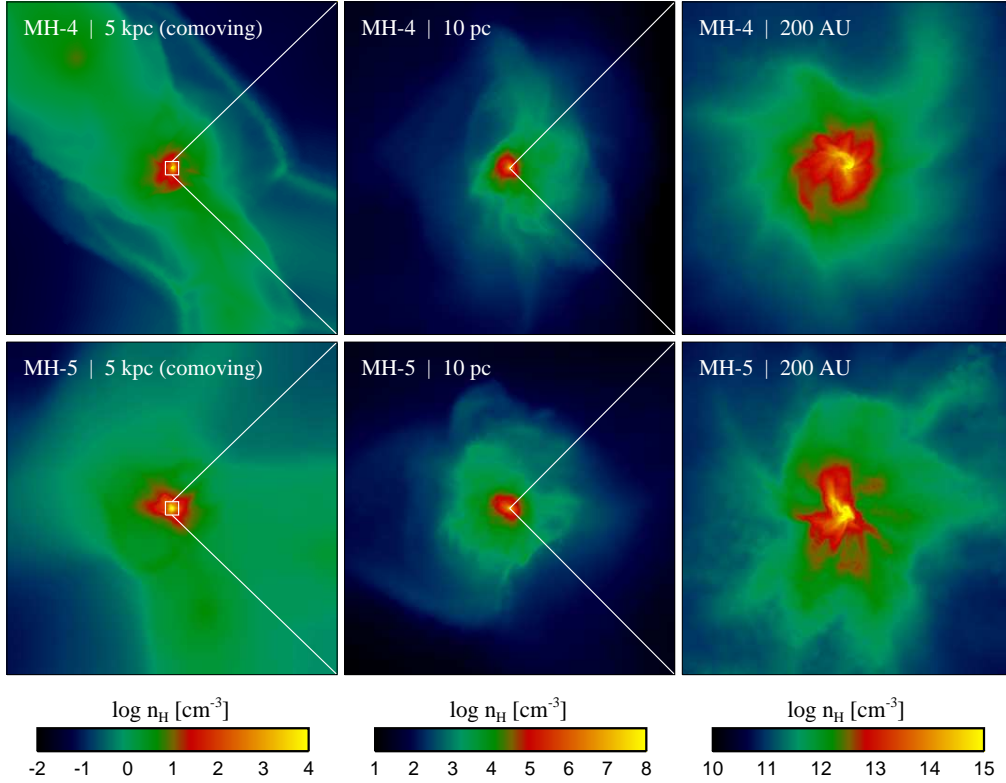


Figure 3. See Figure 2 for caption.

It is well established that an essential prerequisite for reliable hydrodynamic collapse simulations lies in a numerical resolution of the Jeans length. In SPH simulations, the Jeans mass associated with each particle must exceed the mass within the smoothing length by a factor of about two (Bate & Burkert 1997), while grid-based codes rely on the so-called ‘Truelove criterion’ for satisfying this requirement (Truelove et al. 1998), which stipulates that at least four cells per Jeans length should be used. During a collapse simulation, the local resolution must be increased if needed such that the Jeans length stays resolved, otherwise artificial fragmentation may result.

The addition of cells in grid codes is comparatively straightforward, while special care must be taken in SPH simulations to avoid substantial noise when new particles are inserted (Kitsionas & Whitworth 2002). In AREPO, a very simple and robust approach for refinement exists: if a predefined refinement criterion for a cell is fulfilled, the cell is split by inserting a further mesh-generating point at the position of the generator of the original cell, displaced by a random offset that is very small compared to the cell radius. The mass, momentum and energy of the original cell are then distributed conservatively among the two new cells, weighted by their respective volumes, keeping the density, velocity and pressure of the original cell unchanged. Over the course of a few timesteps, the code then separates the mesh-generating points of the two cells and moves them closer to their geometric centers of mass, as a result of the mesh-steering corrections employed by AREPO to maintain a regular structure of the mesh. We note that the numerical fluxes

required for this mesh readjustment arise consistently from the Riemann solutions calculated by the code, as these take the mesh motion fully into account.

We have investigated how the resolution of the Jeans length affects the amount of artificial fragmentation found in AREPO, using a series of isothermal collapse simulations in the formulation of Burkert & Bodenheimer (1993), which is based on a test initially introduced by Boss & Bodenheimer (1979). This setup consists of a $1 M_{\odot}$ cloud with radius $r = 5 \times 10^{16}$ cm and sound speed $c_s = 1.66 \times 10^4$ cm s $^{-1}$ in solid-body rotation with an angular velocity of $\omega = 7.2 \times 10^{-13}$ rad s $^{-1}$ and an $m = 2$ density perturbation of the form

$$\rho(\phi) = \rho_0[1 + 0.1 \cos(2\phi)] , \quad (1)$$

where $\rho_0 = 3.82 \times 10^{-18}$ g cm $^{-3}$ is the underlying constant density and ϕ is the azimuthal angle around the rotation axis. We refine the gas whenever the local Jeans number, here defined as the radius of a cell divided by the local Jeans length, increases above a predefined value. In Figure 1, we show the state of the gas in one of the two main clumps for a minimum of one, two, four, and eight cells per Jeans length. Evidently, artificial fragmentation sets in above a Jeans number of approximately 1/4, which is similar to the result found in AMR codes (Truelove et al. 1998).

In the present study, we activate the refinement criterion in our cosmological simulations above a density of $n_H = 1$ cm $^{-3}$ in the central 200 pc of the halo, which is an upper limit on the virial radius (see Table 1). We ensure that the local Jeans length is always resolved by

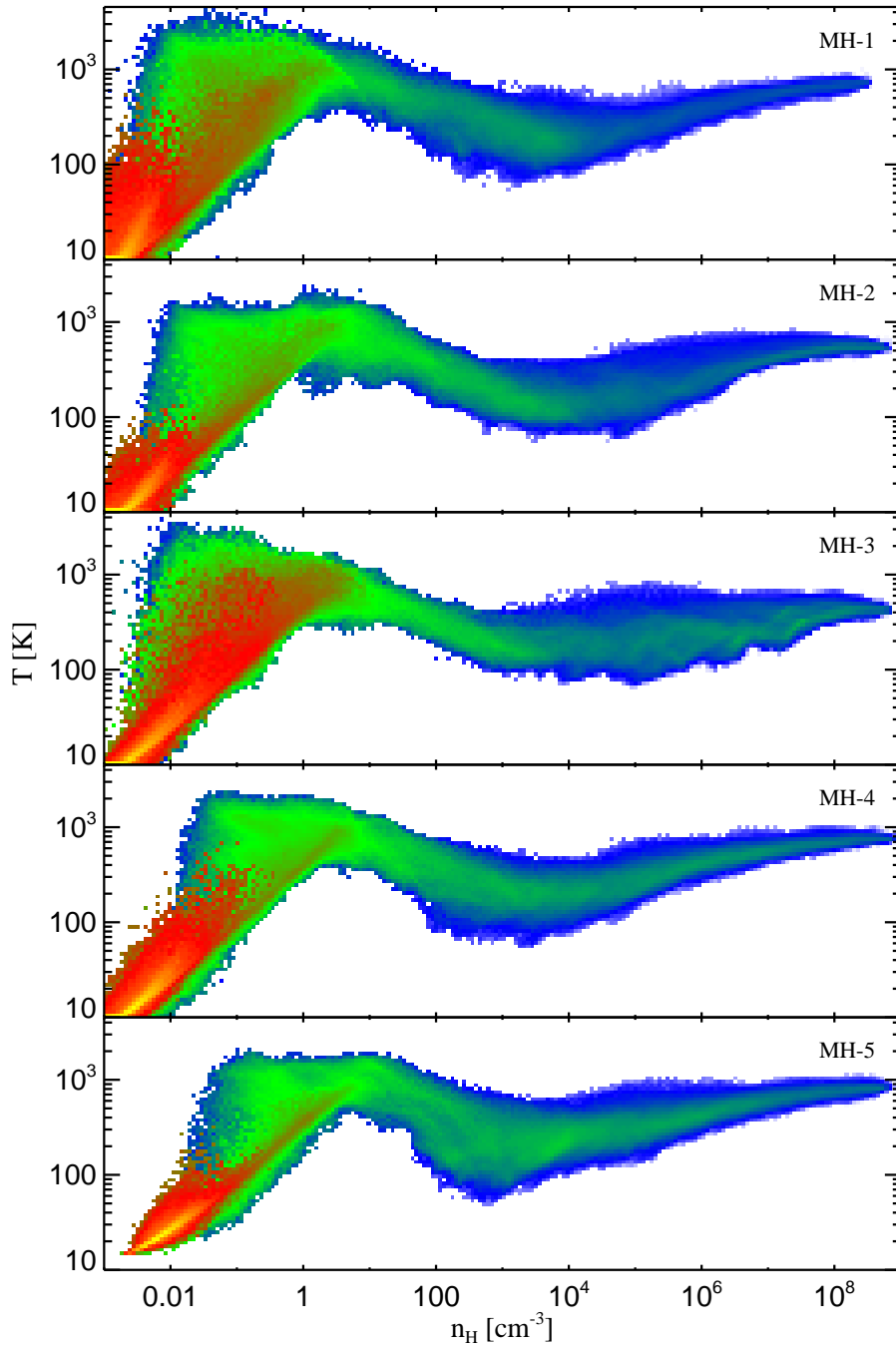


Figure 4. The temperature as a function of hydrogen density in the fully cosmological simulations. The mass in each bin is color-coded from blue (minimum) to yellow (maximum). The evolution of the gas is similar to what was found in previous studies, with the exception that HD cooling becomes important in simulations MH-2 and MH-3, leading to a prolonged cooling phase at $n_{\text{H}} \gtrsim 10^4 \text{ cm}^{-3}$.

at least 128 cells. Once the hydrogen density of the first cell exceeds $n_{\text{H}} = 10^9 \text{ cm}^{-3}$, we extract the central 1 pc of the simulation and reinitialize the simulation in this smaller box with reflective boundary conditions (Springel 2010a). This ensures that the gas remains confined by external pressure. We also discard all DM particles, since the gravitational potential at such high densities is dominated by the gas: About $1000 M_{\odot}$ of gas reside within the central 1 pc, which exceeds the DM mass by at least an order of magnitude. We deactivate the refinement in the resimulations to ensure that the number of cells used

does not increase further, since the particle mass within the central $\simeq 1000 \text{ AU}$ has already dropped to below $10^{-4} M_{\odot}$.

2.5. Sink Particles

The evolution of the gas beyond the runaway collapse of the first protostellar core is captured in our simulations with a sink-particle algorithm that exploits the hybrid nature of AREPO. Since the mesh-generating points are Lagrangian tracers of the fluid, sink particles may be treated very similarly to implementations commonly

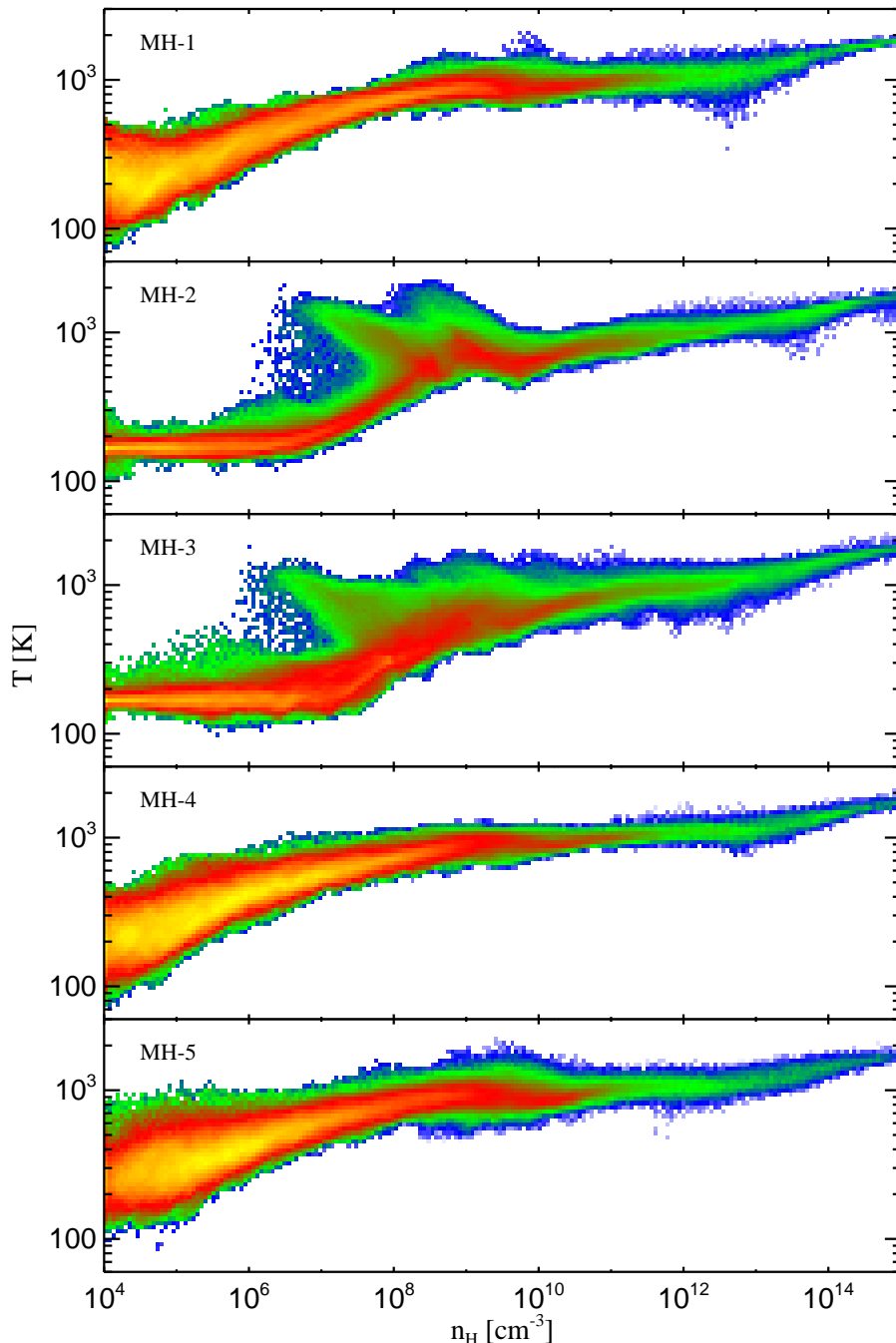


Figure 5. The temperature as a function of hydrogen density for the follow-up high resolution simulations. The mass in each bin is color-coded from blue (minimum) to yellow (maximum). In simulations MH-2 and MH-3, the gas heats up more violently after the prolonged cooling phase due to HD cooling, which creates shocks that are visible as ‘fingers’ of hot, underdense gas. At densities greater than $\sim 10^{16} \text{ cm}^{-3}$, the gas becomes optically thick to cooling radiation and shortly thereafter forms a protostar.

used in SPH simulations (Bate et al. 1995; Jappsen et al. 2005). However, instead of using a density threshold, we identify candidate sink particles whenever the Jeans number of a cell falls below a predefined critical Jeans number $J_{\text{crit}} = 1/8$. For a sink particle to form, the gas within $r_{\text{sink}} = h/J_{\text{crit}}$, where h is the cell radius, is further required to be bound and have a negative velocity divergence. All mesh-generating points within r_{sink} are then removed and replaced by a collisionless sink particle with a gravitational softening length of $r_{\text{acc}}/3$, where r_{acc}

is a predefined accretion radius that is set independently from the initial sink particle radius. In practice, only $\simeq 200$ mesh-generating points are removed during this step, since the spatial resolution around the sink particle decreases at larger radii. The sink particle is placed at the center of mass of the removed cells with a velocity determined by linear momentum conservation, while the angular momentum and internal energy of the gas are discarded. The additional factor $1/3$ in the gravitational softening is used to avoid artificial fragmentation, which

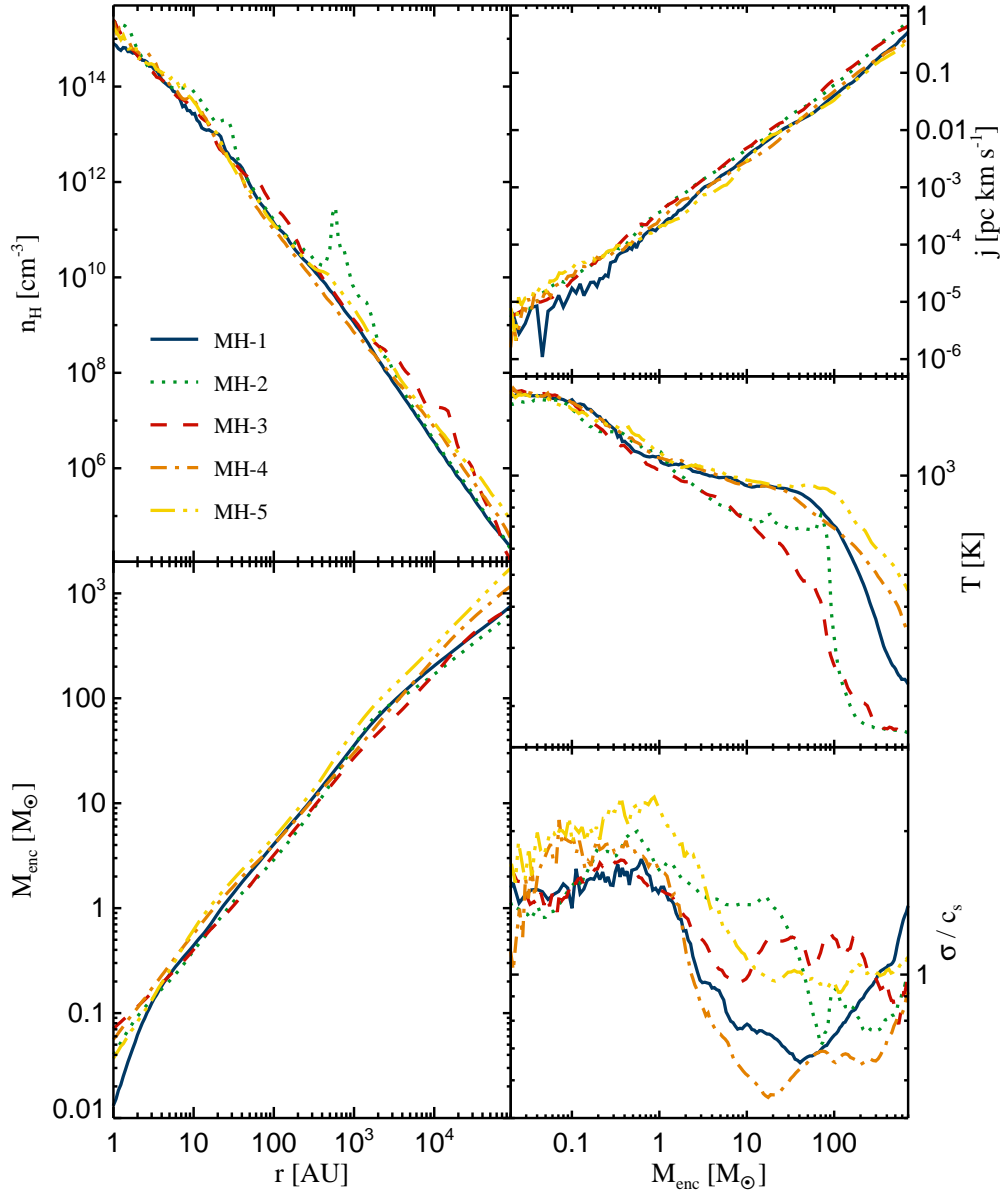


Figure 6. The panels on the left show the spherically averaged hydrogen density and enclosed gas mass as a function of radius just before the formation of the first protostar. The panels on the right show the spherically averaged specific angular momentum, temperature, and velocity dispersion in units of the sound speed as a function of enclosed gas mass. The density, enclosed gas mass, and angular momentum profiles are very similar overall, while the thermal evolution of the gas displays some scatter due to the activation of HD cooling in simulations MH-2 and MH-3. In these two minihalos, the gas heats up later but more violently after becoming gravitationally unstable. The velocity dispersion shows no convincing correlation with the thermal history of the gas and is always close to Mach numbers $M \simeq 1$, indicating transsonic turbulence. Another interesting feature is the simultaneous collapse of a second gas cloud in simulation MH-2, which is visible as a density peak at about 1000 AU from the primary cloud. Similar behavior was found in another recent study (Turk et al. 2009).

might occur if gravitational forces on the gas are reduced on the scale of the accretion radius.

Accretion onto existing sink particles occurs if the mesh-generating point associated with a candidate cell falls within the accretion radius r_{acc} of the sink particle it is most bound to. This method exploits the Lagrangian nature of the mesh-generating points, and yields the (incremental) rate at which mass flows onto sink particles. We have also tested an implementation with a more stringent criterion, where in addition to being bound to the sink particle, the semimajor axis of the respective two-

body system must fall below the accretion radius. However, we have found that these additional criteria made no appreciable difference in practice.

Once a cell has been accreted, its mass and momentum is added to the sink particle and the corresponding mesh-generating point is removed. After this step has been performed for all candidate cells, the mesh is reconstructed such that the volume associated with the removed cells is distributed among the remaining cells around the sink particle. As conserved quantities are weighted with the new volumes, this tends to make

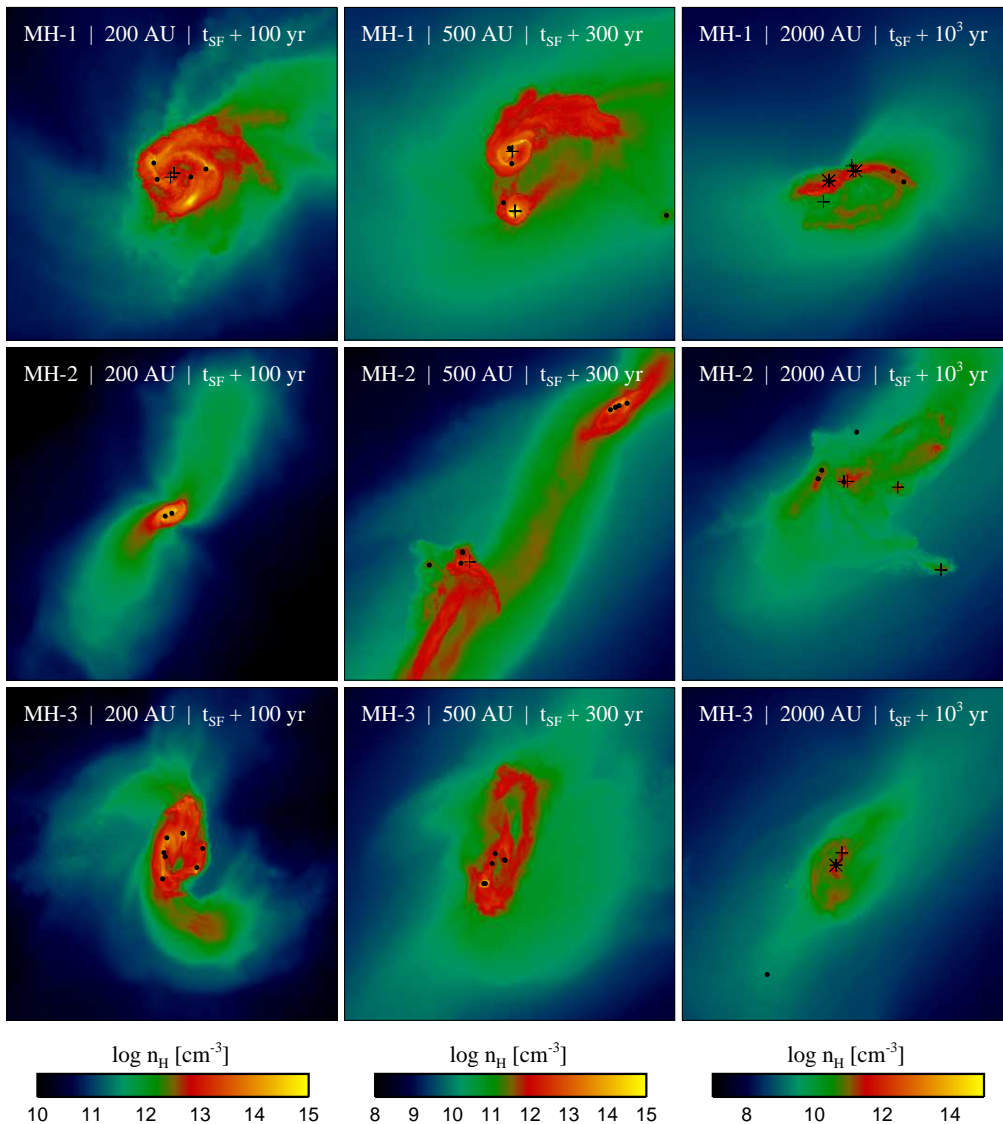


Figure 7. The state of the central gas cloud at various times after the formation of the first protostar, using our standard implementation of sink particles. Shown is the density-squared weighted hydrogen density projected along the line of sight. Black dots, crosses and stars denote protostars with masses below $1 M_{\odot}$, between $1 M_{\odot}$ and $3 M_{\odot}$, and above $3 M_{\odot}$. In all five minihalos, the gas fragments into a relatively rich cluster of protostars with a range of masses. Dynamical interactions can lead to the ejection of low-mass protostars, while more massive protostars tend to remain at the center of the cloud and continue to accrete from the surrounding envelope. A particularly interesting case is simulation MH-2, where two independent clumps collapse almost simultaneously and form their own clusters before eventually merging.

their densities and pressures artificially small. In the last section, we present a resolution study with varying accretion radii to show that this caveat artificially reduces the amount of fragmentation, and increases the typical fragment mass. As our fiducial accretion radius, we choose a value of $r_{\text{acc}} = 100 R_{\odot}$, which is close to the maximum physical size of accreting Pop III stars (Hosokawa & Omukai 2009).

Mergers between sink particles occur whenever the total energy of the respective two-body system is negative and the semimajor axis falls below the accretion radius. This is motivated by our above choice, which yields an approximate upper limit on the physical size of the pro-

tostars. In cases where more than one sink particle lies within the accretion radius of another sink particle, the pair with the highest binding energy merges. For comparison, we have also implemented an alternative, ‘sticky’ merging criterion, where sink particles merge whenever their separation drops below r_{acc} , and no further checks on their energies are enforced. The purpose of this formulation is to maximize the efficiency of merging between protostars, since we do not capture the gasdynamical friction between real protostars.

2.6. Chemistry and Cooling

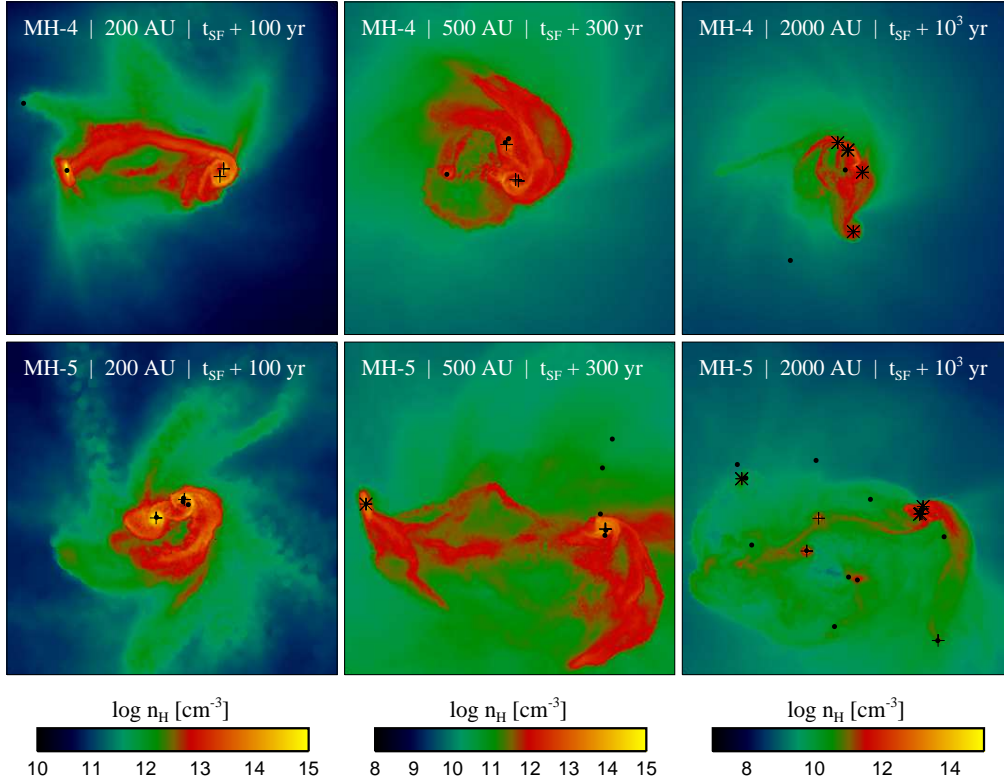


Figure 8. See Figure 7 for caption.

The chemical evolution of the gas is modeled with a primordial chemistry network consisting of 45 reactions amongst twelve chemical species: H, H⁺, H⁻, H₂⁺, H₂, He, He⁺, He⁺⁺, D, D⁺, HD, and free electrons (Clark et al. 2011). We account for all relevant cooling processes, including electronic excitation of H, He and He⁺, cooling from the recombination of H⁺ and He⁺, Compton cooling, and bremsstrahlung. In practice only a few processes play an important role at the densities and temperatures investigated here – H₂ rotational and vibrational line cooling, H₂ collision-induced emission (CIE) cooling, H₂ collisional dissociation cooling, and heating due to three-body H₂ formation (see also Turk et al. 2011).

We model H₂ line cooling in the optically thin regime using the low-density cooling rates for collisions between H₂ molecules and H and He atoms, H₂ molecules, protons and electrons (Glover & Abel 2008), and account for the transition to local thermodynamic equilibrium level populations at gas densities $n_{\text{H}} \gg 10^4 \text{ cm}^{-3}$. At densities above $n_{\text{H}} \sim 10^9 \text{ cm}^{-3}$, the strongest of the H₂ ro-vibrational lines become optically thick, reducing the effectiveness of H₂ line cooling. To account for this effect, we use an approach based on the Sobolev approximation (Yoshida et al. 2006). We write the H₂ cooling rate as

$$\Lambda_{\text{H}_2} = \sum_{u,l} \Delta E_{ul} A_{ul} \beta_{\text{esc},ul} n_u, \quad (2)$$

where n_u is the number density of hydrogen molecules in upper energy level u , ΔE_{ul} is the energy difference between this upper level and a lower level l , A_{ul} is the spon-

taneous radiative transition rate for transitions between u and l , and $\beta_{\text{esc},ul}$ is the escape probability associated with this transition, i.e. the probability that the emitted photon can escape from the region of interest. We fix n_u by assuming that the H₂ level populations are in local thermodynamic equilibrium, and write the escape probabilities for the various transitions as

$$\beta_{\text{esc},ul} = \frac{1 - \exp(-\tau_{ul})}{\tau_{ul}}, \quad (3)$$

where we use the approximation that

$$\tau_{ul} \simeq \alpha_{ul} L_s, \quad (4)$$

where α_{ul} is the line absorption coefficient and L_s is the Sobolev length (Yoshida et al. 2006). In the classical, one-dimensional spherically symmetric case, the Sobolev length is given by

$$L_s = \frac{v_{\text{th}}}{|dv_r/dr|}, \quad (5)$$

where v_{th} is the thermal velocity, and dv_r/dr is the radial velocity gradient. In our three-dimensional simulations, we generalize this as (Neufeld & Kaufman 1993)

$$L_s = \frac{v_{\text{th}}}{|\nabla \cdot \mathbf{v}|}. \quad (6)$$

To prevent the H₂ cooling rate from being reduced by an unphysically large amount in regions with small velocity gradients, we limit L_s to be less than or equal to the local Jeans length, L_J . We justify this choice by noting that there are strong density gradients in the gas on scales

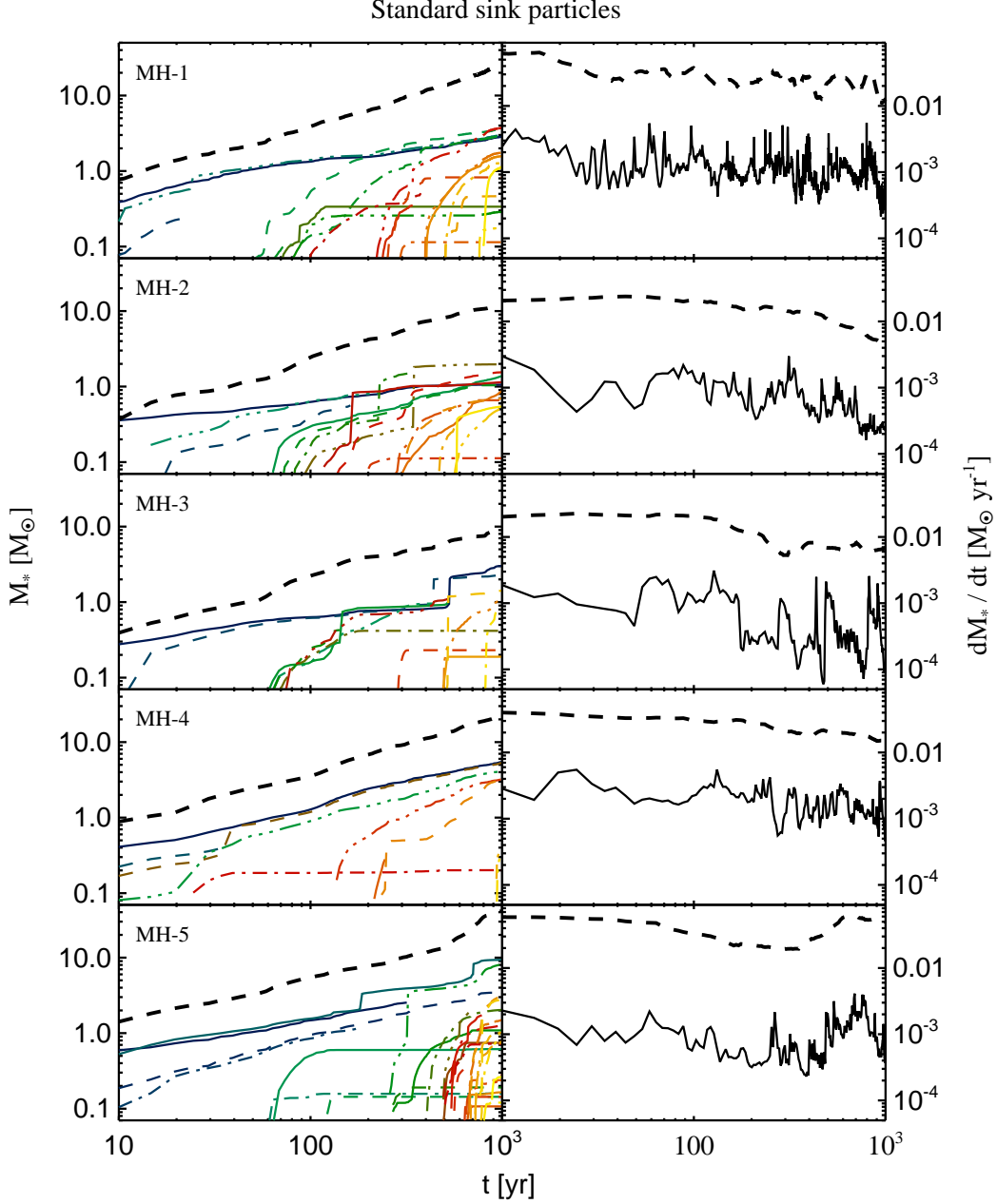


Figure 9. The mass accretion histories of the protostars (left panels), and the average accretion rates of the entire ensemble of protostars (right panels), assuming our standard formulation of sink particles. In the left panels, each line denotes the evolution of an individual protostar. The thick dashed lines in both panels denote the cumulative values. Mergers are indicated by instantaneous jumps in mass. We find that star formation is not restricted to a single burst, but occurs continually for the entire simulated timespan. In every minihalo, between 5 and 15 protostars with masses ranging from 0.1 to nearly $10 M_{\odot}$ are formed. The total accretion rates are nearly constant over time at a few $0.01 M_{\odot} \text{ yr}^{-1}$.

$L \gg L_J$, and so we expect the bulk of the contribution to the H_2 line absorption to come from material within only a few Jeans lengths.

At very high densities ($n_{\text{H}} > 10^{14} \text{ cm}^{-3}$), CIE cooling from H_2 becomes more effective than H_2 line cooling (Ripamonti & Abel 2004). We account for the reduction of the CIE cooling rate due to the effects of continuum opacity using the following prescription (Ripamonti & Abel 2004):

$$\Lambda_{\text{CIE,thick}} = \Lambda_{\text{CIE,thin}} \min\left(\frac{1 - e^{-\tau_{\text{CIE}}}}{\tau_{\text{CIE}}}, 1\right), \quad (7)$$

where

$$\tau_{\text{CIE}} = \left(\frac{n_{\text{H}}}{1.4 \times 10^{16} \text{ cm}^{-3}}\right)^{2.8}. \quad (8)$$

Finally, we account for the fact that each time an H_2 molecule is collisionally dissociated, 4.48 eV of thermal energy is lost by the gas, while every time that a new H_2 molecule is formed by the three-body process, the gas gains 4.48 eV.

3. RESULTS

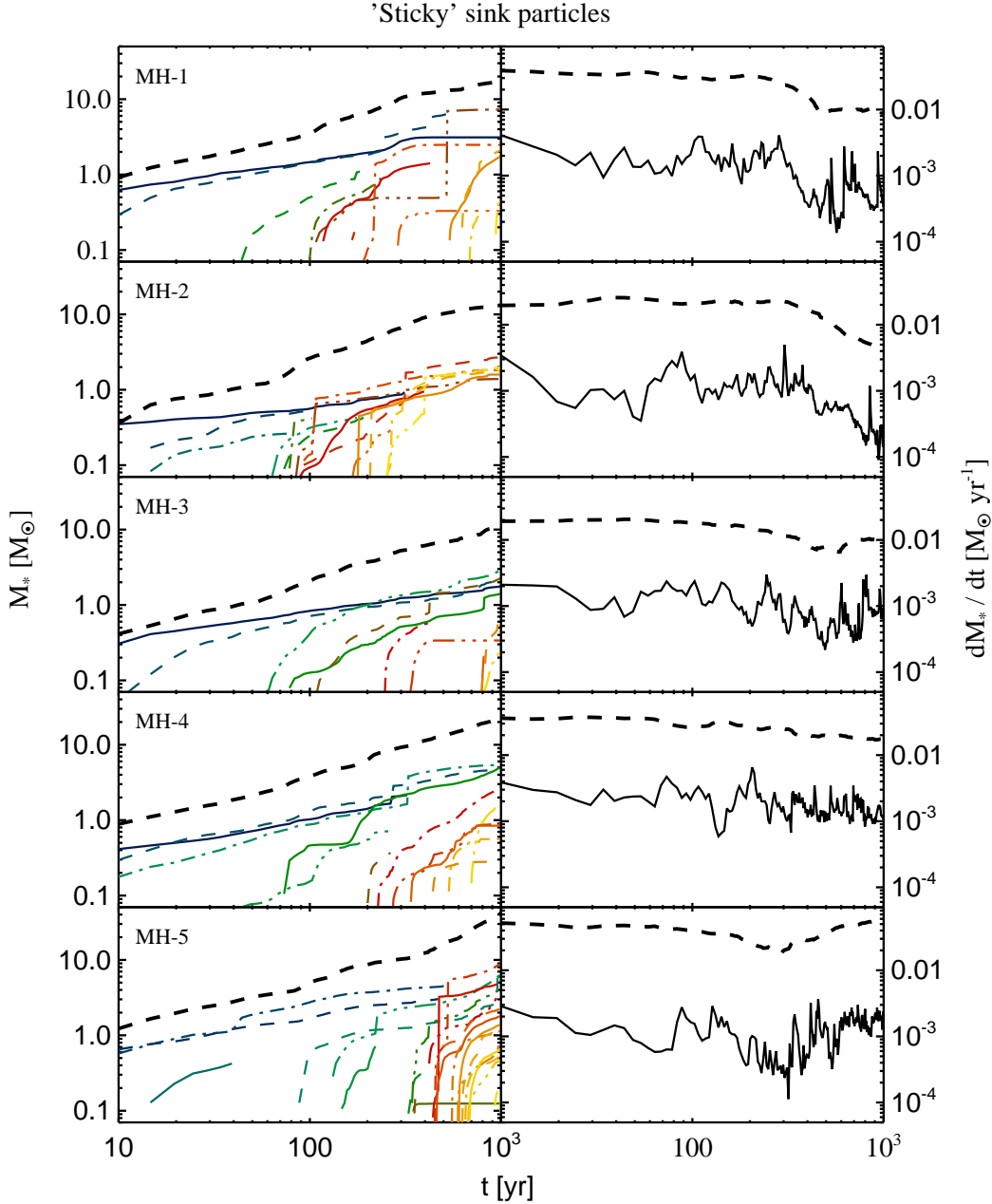


Figure 10. The same as Figure 9, but with ‘sticky’ sink particles. Compared to the case with standard sink particles, fewer protostars with systematically higher masses are formed. However, the total amount of gas locked up in sink particles is nearly identical.

We here discuss the collapse of the gas in the minihalos up to the formation of the first protostar, and the subsequent fragmentation and accretion that leads to the build-up of the protostellar cluster. We then proceed to investigate the effects of radiation feedback, the variation of the accretion radius, and the neglect of gasdynamical friction between protostars.

3.1. Collapse of Gas in Minihalos

In Figures 2 and 3, we show the collapse of the gas in all five minihalos from cosmological to protostellar scales. As gas falls into the DM halo, shocks thermalize the gravitationally generated infall motions and heat the gas to the halo virial temperature. At the same time, irregu-

lar motions of the dark matter seed subsonic turbulence in the gas, which cascades down to ever smaller scales and later influences the fragmentation of the protostellar cloud. Once enough hydrogen molecules have formed, the gas at the center of the halo begins to cool, eventually becoming gravitationally unstable and decoupling from the dark matter on scales below 10 pc (Abel et al. 2002; Bromm et al. 2002). At significantly higher densities, three-body reactions render the gas fully molecular in a region of size a few hundred AU (Yoshida et al. 2006). Somewhat later, the gas becomes optically thick and the cooling radiation can no longer escape, inducing a final heating phase that ends with the formation of a protostar (Yoshida et al. 2008). At this point a sink par-

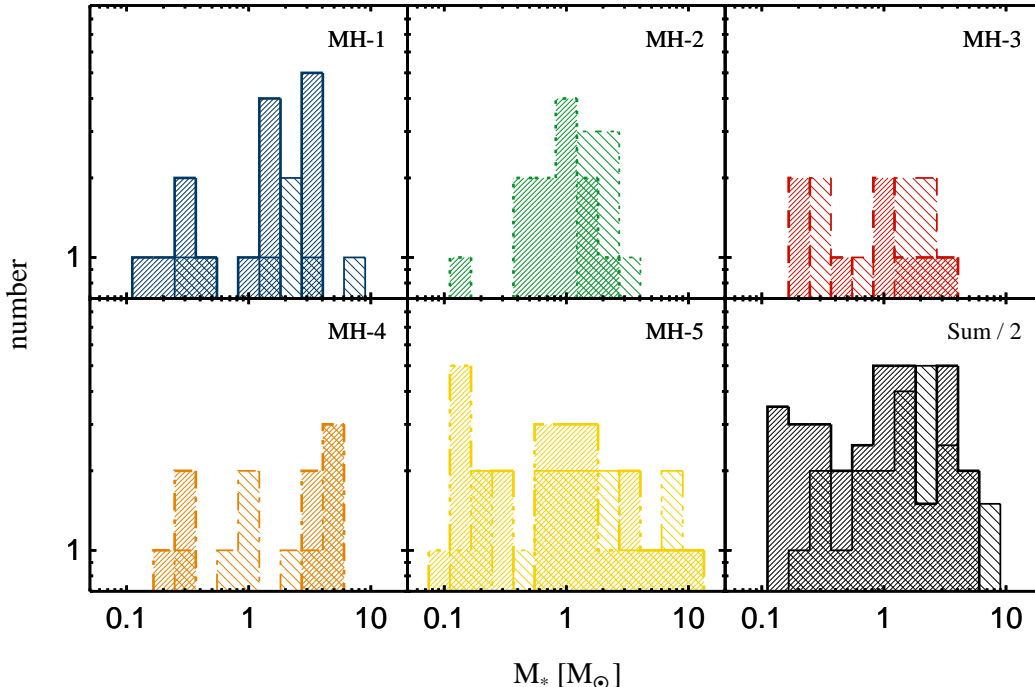


Figure 11. The protostellar mass function after 1000 years of continued fragmentation and accretion. The dark and light shadings distinguish mass functions obtained for standard and ‘sticky’ sink particles, respectively. Despite very aggressive merging, a small cluster of protostars with a range of masses is formed even for ‘sticky’ sink particles. In the bottom right panel, we also show the cumulative functions obtained by summing up the contributions from the individual minihalos, and renormalized for better visibility. The resulting distribution is relatively flat between ~ 0.1 and $\sim 10 M_{\odot}$, indicating that most of the mass is locked up in high-mass protostars.

ticle with an accretion radius of 100 solar radii is inserted, close to the photospheric size of the accreting protostar (Hosokawa & Omukai 2009).

Although the evolution of the gas is quite similar in all cases, some scatter in the thermal history exists (see also O’Shea & Norman 2007). In simulations MH-2 and MH-3, HD cooling becomes important and leads to a prolonged cooling phase at densities $n_{\text{H}} \gtrsim 10^4 \text{ cm}^{-3}$ (Ripamonti 2007; McGreer & Bryan 2008). This is evident from Figures 4 and 5, where we show the occupation of the gas in density and temperature space. There is no correlation of the prolonged cooling with the bulk properties of the underlying DM halo (see Table 1), indicating that details of the virialization process must be responsible for this effect. Note that the temperature floor required for HD cooling is around 150 K, which is only marginally attained in most minihalos. The activation of HD cooling is therefore very sensitive to the evolution of the gas during the initial free-fall phase. A second interesting effect is the shock-heating of some parcels of gas, which we attribute to the more violent heating in simulations MH-2 and MH-3 once three-body reactions set in.

In Figure 6, we show the internal structure of the minihalos just before the formation of the first protostar. The density, enclosed mass, and angular momentum profiles are relatively similar and agree well with previous investigations (Abel et al. 2002; Yoshida et al. 2006). The density peak observable in simulation MH-2 indicates the nearly simultaneous collapse of a second gas cloud, which was also found in Turk et al. (2009). The temperature profiles shows significant scatter due to the previously mentioned differences in the virialization process. We

find no convincing correlation of the thermal history of the gas with the velocity dispersion. The latter is always close to Mach numbers $M \simeq 1$, which indicates transsonic turbulence.

3.2. Fragmentation and Protostellar Mass Function

Shortly after the first protostar has formed, the residual angular momentum of the surrounding gas cloud leads to the formation of a circumstellar accretion disk. Since the infall rate of new material onto the disk is extremely high, angular momentum transport by viscous and gravitational torques is not sufficient to prevent the disk from fragmenting. As shown in the left panels of Figures 7 and 8, the disk hence passes the gravitational instability limit, at which point it forms a number of secondary protostars. After this initial burst, the gas becomes gravitationally unstable multiple times and forms a small cluster of ~ 10 protostars after only 1000 yr.

The complex gravitational interactions between individual protostars and the surrounding gas clouds are illustrated in Figures 9 and 10, where we show the mass accretion histories of the protostars for two different sink-particle schemes. In our standard approach, sink particles merge if they become gravitationally bound and pass within 100 solar radii of each other, while in our alternative, ‘sticky’ formulation, only the latter criterion must be fulfilled. The second model is a crude representation of the dissipative effects of shocks in collisions between physically extended protostars. Both techniques have been used in (radiation) hydrodynamic simulations of star cluster formation in the present-day universe (Klessen & Burkert 2000; Bate et al. 2003; Krumholz et al. 2009; Federrath et al. 2010; Peters et al.

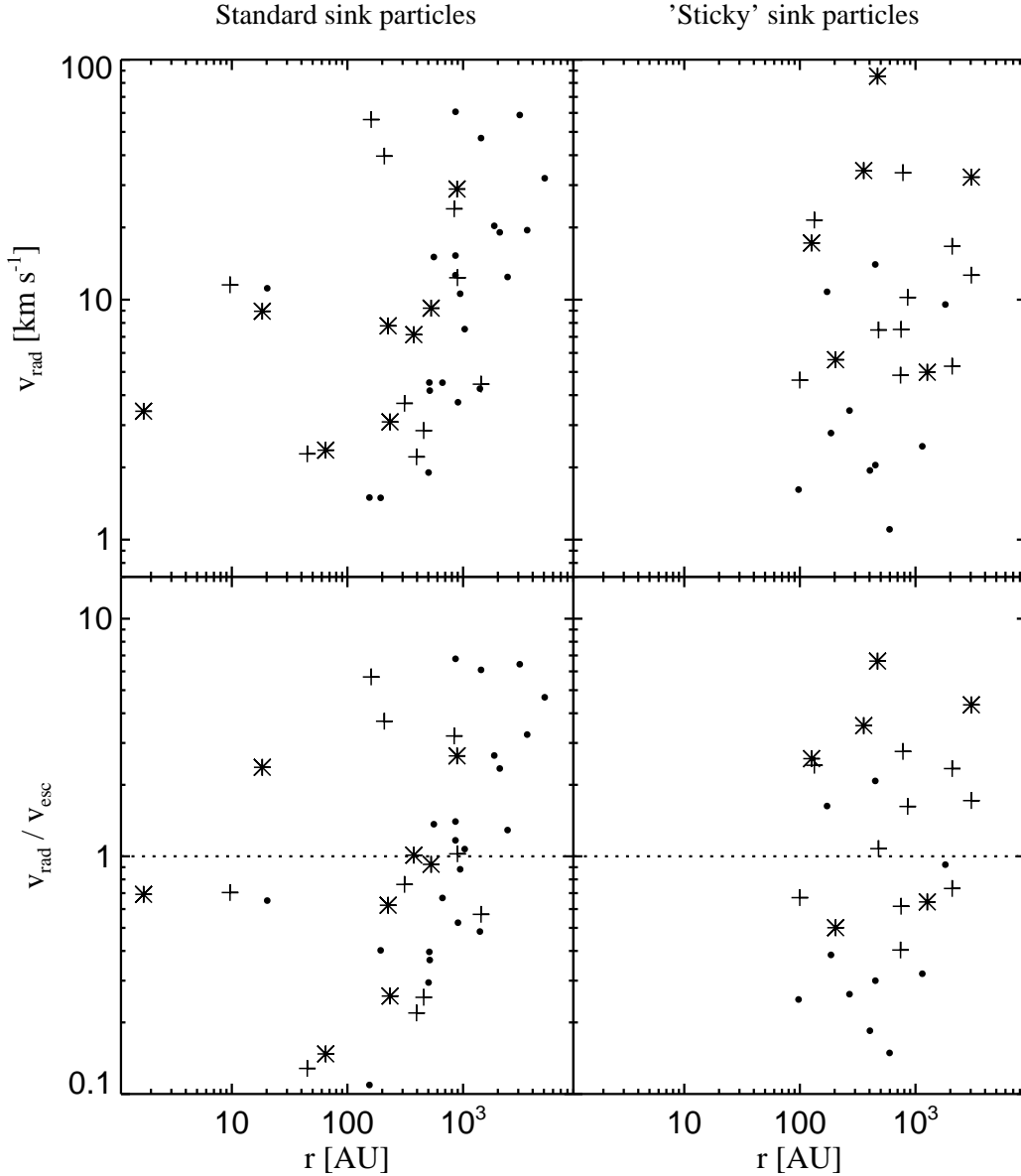


Figure 12. The radial velocity and ratio of the radial velocity to the escape velocity of all protostars as a function of distance to the center of mass, shown for standard (left panels) and ‘sticky’ (right panels) sink particles. The critical ratio of unity, where protostars are assumed to escape from the central gas cloud, is denoted by the dashed line. The escape velocity is determined by using the total mass enclosed within the current distance of each protostar from the center of mass. Black dots, crosses and stars denote protostars with masses below $1 M_{\odot}$, between $1 M_{\odot}$ and $3 M_{\odot}$, and above $3 M_{\odot}$. In our standard implementation of sink particles, a number of low-mass protostars obtain high radial velocities and escape from the central gas cloud. They stop accreting after they receive substantial radial velocities during close encounters with other protostars, and might therefore enter the main sequence as low-mass Pop III stars. In our ‘sticky’ implementation of sink particles, this occurs significantly less often. Furthermore, no protostars reside within the central $\simeq 100$ AU, since momentum conservation acts to move newly merged protostars to larger radii.

2010). In the absence of a detailed understanding of the true protostellar radii and the influence of tidal forces during close encounters, we may hope that they bracket physical reality.

Interestingly, the two methods predict nearly identical total protostellar masses, but yield different detailed mass accretion histories. In our standard formulation of sink particles, protostars generally survive close encounters, whereas in our ‘sticky’ formulation these interactions often result in a merger. For this reason the number of protostars after 1000 yr is higher in our standard

formulation of sink particles than in our ‘sticky’ formulation. This is evident from Figure 11, where we show the final protostellar mass functions of all five mini-halos. Notably, a small group of protostars with a range of masses is formed in both sink-particle formulations. The cumulative protostellar mass functions obtained from the five independent realizations are relatively flat, extending from $\sim 0.1 M_{\odot}$ to nearly $10 M_{\odot}$ (bottom right panel of Figure 11). This corresponds to a top-heavy mass function, in the sense that most of the protostellar mass is locked up in massive protostars.

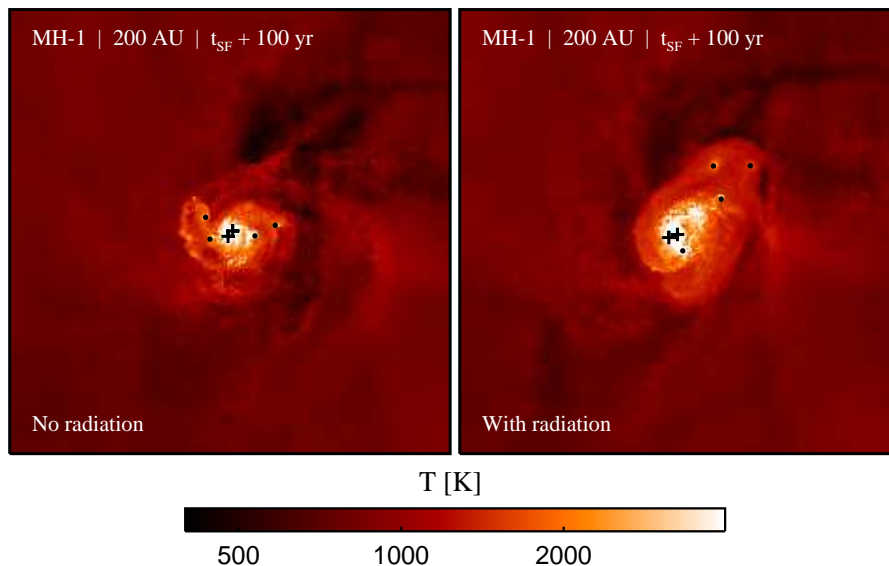


Figure 13. A comparison of the fragmentation of the gas in simulation MH-1 with and without infrared radiation emitted by accreting protostars. The panels show the density-squared weighted temperature projected along the line of sight. The radiation slightly heats and puffs up the disk, such that the fragments form at somewhat larger distances from the center. The qualitative nature of radiation feedback is therefore very similar to what is found in studies of present-day star formation (Krumholz et al. 2009; Peters et al. 2010), although the effect is significantly reduced due to the very efficient cooling by molecular hydrogen lines.

A trend particularly evident in our standard formulation of sink particles is that some low-mass protostars are ejected from the central gas cloud by dynamical interactions with more massive protostars, while the latter tend to remain at the center of the minihalo and continue to accrete at a high rate. This is also visible in Figure 12, where we show the radial velocity and ratio of the radial velocity to the escape velocity of all protostars. A number of protostars move away from the center of mass with speeds exceeding the escape velocity, such that they stop accreting and might enter the main sequence as low-mass Pop III stars. This does not occur as often in our formulation of ‘sticky’ sink particles, where many protostars merge before they can be ejected. We also find that no protostars reside within the central $\simeq 100$ AU, since momentum conservation acts to move newly merged protostars to larger radii.

3.3. Radiation Feedback

Studies of present-day star formation have shown that the radiation emitted from young protostars heats the surrounding envelope and reduces the amount of fragmentation close to the central star (Krumholz et al. 2009; Peters et al. 2010). However, the outcome is less clear in the present study, where gas temperatures are a factor of 10 – 100 times higher and different cooling mechanisms play a role. To investigate the importance of radiation in detail, we compare simulations with and without the heating from accreting Pop III stars in one of the five minihalos.

During the early stages of protostellar evolution, Pop III stars grow rapidly in size from $\simeq 10$ to $\simeq 100 R_{\odot}$ (Hosokawa & Omukai 2009). The temperature of the photosphere remains roughly constant at 6000 K, and so most of the energy is radiated in the optical and infrared. Once the protostar has accreted of order $10 M_{\odot}$, the star undergoes Kelvin-Helmholtz contraction and heats up substantially, leading to the emission of ionizing radi-

ation. Since we are well within the initial swelling phase, we can utilize a simple optically thin treatment of the radiation to determine the maximum extent to which the gas will be affected.

For this purpose we treat each sink particle formed in our simulation as a separate protostar, and account for the energy released by accretion onto the surfaces of these protostars. To model the effects of this accretion luminosity, we first compute the bolometric accretion luminosity for each protostar

$$L_{\text{acc}} = \frac{GM_*\dot{M}_*}{R_*}, \quad (9)$$

where \dot{M}_* is the accretion rate onto the protostar, M_* is the protostellar mass and R_* is the protostellar radius. We relate the protostellar radius to the current protostellar mass and accretion rate using a relationship derived for adiabatically accreting, metal-free protostars embedded in a spherically symmetric inflow (Stahler et al. 1986):

$$R_* = 26 R_{\odot} \left(\frac{M_*}{M_{\odot}} \right)^{0.27} \left(\frac{\dot{M}_*}{10^{-3} M_{\odot} \text{ yr}^{-1}} \right)^{0.41}. \quad (10)$$

More recent calculations for the case of rotating infall find an even larger value for R_* during the adiabatic accretion phase (Tan & McKee 2004), and so using the above expression gives us a conservative upper limit on the bolometric accretion luminosity during this phase.

Combining the above equations, we find that

$$L_{\text{acc}} \simeq 1200 L_{\odot} \left(\frac{M_*}{M_{\odot}} \right)^{0.73} \left(\frac{\dot{M}_*}{10^{-3} M_{\odot} \text{ yr}^{-1}} \right)^{0.59}. \quad (11)$$

With this expression, we determine the heating rate of

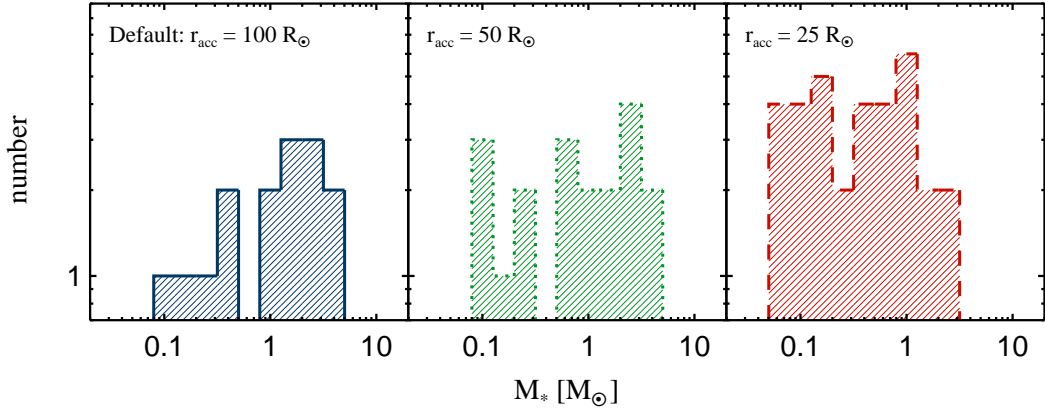


Figure 14. The final mass function of simulation MH-1 for accretion radii decreased by factors of two and four from the fiducial value $r_{\text{acc}} = 100 R_{\odot}$. The collapse of the gas is therefore followed to higher densities and smaller radii around the protostar. Any systematic inaccuracies stemming from the artificially reduced density and pressure around sink particles should therefore induce a systematic trend in this figure. As is evident from the plot, such a trend exists: the amount of fragmentation increases, while the typical mass of a fragment decreases. This strengthens our claim that the generic outcome is a small cluster of protostars with a range of masses.

the gas surrounding the protostar from

$$\Gamma_* = \rho \kappa_p \frac{L_{\text{acc}}}{4\pi r^2}, \quad (12)$$

where ρ is the mass density, r is the distance to the protostar, and κ_p is the Planck mean opacity of the gas. We calculate this mean opacity by interpolation, using tabulated values that account for both line and continuum absorption (Mayer & Duschl 2005), and that include the influence of the electrons provided by ionized lithium. This expression assumes that the gas is optically thin to the radiation from the accreting protostar. Making this assumption allows us to avoid the extremely high computational cost that would be associated with an accurate treatment of the transfer of the protostellar radiation, and also gives us a conservative upper limit on the effectiveness of protostellar feedback. Finally, we assume that each protostar accretes at a rate of $0.1 M_{\odot} \text{ yr}^{-1}$, which is well above the total accretion rate of the whole ensemble of protostars, maximizing the effect of our radiative feedback model.

In Figure 13, we compare simulations with and without radiation feedback for the case of our ‘fiducial’ minihalo MH-1. We find that the additional heating results in a smoother and more extended disk, where the fragments form at slightly larger distances from the center. However, even the unrealistically strong radiation field assumed here does not prevent fragmentation within the disk. The primary reason for this is the strong cooling of the gas by molecular hydrogen lines at temperatures around 1000 K and above, which largely offsets the heating caused by the accretion luminosity. The neglect of radiation in our main simulations should therefore not qualitatively affect our conclusions. We note that a more detailed investigation is presented in a companion paper (Smith et al. 2011). Finally, it is important to point out that the heating may be much more severe once the first protostar has accreted of order $10 M_{\odot}$ and begins to emit ionizing radiation (Tan & McKee 2004; McKee & Tan 2008). However, this will not occur until after the period of time simulated here.

3.4. Variation of Accretion Radius

The removal of mesh-generating points below the accretion radius artificially reduces the density and pressure around sink particles. We investigate the influence of this by systematically decreasing the accretion radius from $100 R_{\odot}$ to $50 R_{\odot}$ and $25 R_{\odot}$. The gas therefore collapses to progressively higher densities before being accreted onto the sink particle, such that any residual effects should display a trend in the total number and mass spectrum of fragments formed. As is evident from Figure 14, such a trend exists: A reduction of the accretion radius results in an increase in the number of fragments and a decrease of the typical fragment mass. Existing sink particles apparently accrete less aggressively, such that more mass remains in the disk, which in turn becomes even more susceptible to fragmentation. This trend lends further support to our claim that Pop III protostars formed in clusters and had a range of masses.

3.5. Protostellar Merging

Another limitation of the sink-particle algorithm employed here is that the gasdynamical friction between physically extended protostars is not modeled. Mergers between protostars may therefore be more common than we find using purely gravitationally interacting sink particles. To understand the importance of this effect in more detail than was possible with our ‘sticky’ sink-particle formulation, we use Equation 10 to compare the minimum separation of each protostar to any other protostar with the sum of the protostellar radii during their closest encounter. Figure 15 shows that the majority of protostars experience at least one close encounter with another protostar and, depending on the eccentricity and infall velocity of the respective orbit, will merge. However, it is also evident that a few low-mass protostars remain physically well separated for the entire duration of the simulation, while acquiring substantial radial velocities (see Figure 12). As mentioned already in Section 3.2, these protostars stop accreting and may therefore enter the main sequence as low-mass Pop III stars. A more accurate account would require simulations that self-consistently capture the interaction of the protostars with the surrounding gas cloud. These are not currently feasible.

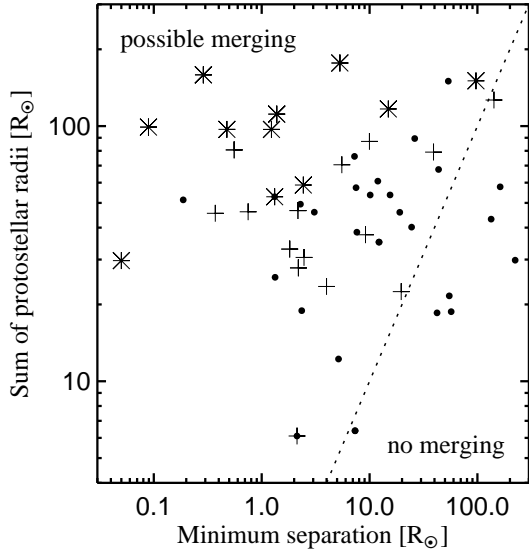


Figure 15. We obtain a more accurate account of merging by comparing the minimum separation of each protostar to any other protostar with the sum of the protostellar radii during their closest encounter. Black dots, crosses and stars denote protostars with masses below $1 M_{\odot}$, between $1 M_{\odot}$ and $3 M_{\odot}$, and above $3 M_{\odot}$. Nearly all protostars with masses above $1 M_{\odot}$ experience at least one encounter with another protostar where the separation drops below their total physical size. Depending on the eccentricity and infall velocity of the respective orbits, they could then merge. However, a number of low-mass protostars also remain physically well separated for the entire duration of the simulation, while receiving substantial radial velocities (see also Figure 12). It is therefore possible that some of these will enter the main sequence as low-mass Pop III stars.

4. SUMMARY AND CONCLUSIONS

We have used the moving mesh code AREPO to follow the runaway collapse of the gas in five statistically independent minihalos from cosmological to protostellar scales – over more than twenty orders of magnitude in density. We have captured the subsequent evolution of the newborn protostellar cloud for more than 100 dynamical times with a sink-particle algorithm that resolves the accretion of the gas down to scales of $100 R_{\odot}$ or less, comparable to the maximum physical size of Pop III protostars. In all five minihalos, a circumstellar disk forms that fragments vigorously into a small cluster of protostars with a range of masses. The gas becomes gravitationally unstable multiple times and continues to form protostars for the entire duration of the simulation. After only 1000 yr of accretion, of order 10 protostars per minihalo have formed and display a relatively flat protostellar mass function ranging from ~ 0.1 to nearly $10 M_{\odot}$.

Although the sink-particle technique employed in this study allows a continuation of the calculations to much later times than was possible in previous *ab initio* simulations of primordial star formation (Abel et al. 2002; Yoshida et al. 2008), a number of uncertainties remain. One problem is the artificially reduced density and pressure created by the removal of mesh-generating points near sink particles. However, the variation of accretion radii discussed in Section 3.4 shows that this effect reduces the amount of fragmentation and increases the typical fragment mass. A correct treatment of the boundary

region between sink particles and the gas should therefore strengthen our conclusions. A more important caveat is the inability of the sink particle algorithm to model the gasdynamical friction between physically extended protostars during close encounters. In an attempt to maximize the impact of this effect, we have implemented ‘sticky’ sink particles in addition to our standard sink-particle algorithm. As was shown in Section 3.2, this leads to an increased merger rate, so that fewer protostars survive. However, even this extreme assumption does not prevent the gas from forming a cluster of protostars. In addition, the results presented in Section 3.5 show that a number of protostars never experience close encounters. A final caveat is that we do not self-consistently model the interaction of the protostars with the surrounding gas. It is unclear how important the resulting neglect of gasdynamical friction and torques is, since simulations that model the protostellar surface as well as the parent gas cloud are not yet feasible. However, it appears unlikely that this caveat will qualitatively affect our conclusions, since fragmentation takes place on scales significantly larger than the resolution length.

Modulo the uncertainties mentioned above, the simulations presented here portray a very different picture of primordial star formation than is commonly assumed. Instead of forming a single object, the gas in minihalos fragments vigorously into a number of protostars with a range of masses. It is an open question as to how this early mass function will be mapped into the final mass function of Pop III, after accretion, fragmentation and merging have finally stopped. However, it is interesting to speculate how this nonlinear mapping will play out. If a flat, broad mass function persists, a number of lower-mass Pop III stars will have formed which could survive to the present day if their mass remains below $\sim 0.8 M_{\odot}$. Although this possibility is speculative because of the above uncertainties and the fact that we follow the protostellar accretion only for the first 1000 out of 10^5 or 10^6 yr, it is worth looking for such Pop III fossils in ongoing and planned large surveys of metal-poor stars in the Milky Way (Beers & Christlieb 2005).

Furthermore, the presence and mutual competition of multiple accretors in a given minihalo will act to limit the growth of the most massive objects. Pop III stars are therefore less likely to reach masses in excess of $\sim 140 M_{\odot}$, the threshold for triggering extremely energetic pair-instability supernovae (PISNe) during stellar death (Heger & Woosley 2002). A reduced PISN rate is more easily compatible to the absence of their distinct nucleosynthetic signatures in any of the extremely metal-poor halo stars observed so far (Iwamoto et al. 2005). Pop III stars could still have given rise to numerous extremely luminous supernova explosions, if they had masses of a few $10 M_{\odot}$ and if they were rapid rotators, as suggested by recent studies (Stacy et al. 2010a). They would then have exploded as core-collapse hypernovae, with explosion energies that are similar to PISNe (Umeda & Nomoto 2002). Finally, our results may challenge models of so-called ‘dark stars’, which are Pop III stars powered by dark matter self-annihilation heating (Freese et al. 2008; Iocco et al. 2008). These models invoke an increased DM interaction rate at the center of the Pop III star which itself lies at rest at the center of its minihalo. The complex dynamics of a protostellar

cluster at the center of the minihalo may preclude such efficient DM capture and heating.

T.H.G. thanks Klaus Dolag for support on numerous technical issues, and Tom Abel and Naoki Yoshida for many stimulating discussions. We thank the Leibniz Supercomputing Center of the Bavarian Academy of Sciences and Humanities, and the Computing Center of the Max-Planck-Society in Garching, where the simulations were carried out. R.S.K. acknowledges financial support from the *Baden-Württemberg Stiftung* via their program International Collaboration II (grant P-LS- SPII/18) and from the German *Bundesministerium für Bildung und Forschung* via the ASTRONET project STAR FORMAT (grant 05A09VHA). R.S.K. furthermore acknowledges subsidies from the DFG under grants no. KL1358/1, KL1358/4, KL1358/5, KL1358/10, and KL1358/11, as well as from a Frontier grant of Heidelberg University sponsored by the German Excellence Initiative. V.B. acknowledges support from NSF grants AST-0708795 and AST-1009928, as well as NASA through Astrophysics Theory and Fundamental Physics Program grants NNX 08-AL43G and 09-AJ33G.

REFERENCES

- Abel, T., Bryan, G. L., & Norman, M. L. 2002, *Science*, 295, 93
 Agertz, O., et al. 2007, *MNRAS*, 380, 963
 Barkana, R., & Loeb, A. 2001, *Phys. Rep.*, 349, 125
 Bate, M. R., Bonnell, I. A., & Bromm, V. 2003, *MNRAS*, 339, 577
 Bate, M. R., Bonnell, I. A., & Price, N. M. 1995, *MNRAS*, 277, 362
 Bate, M. R., & Burkert, A. 1997, *MNRAS*, 288, 1060
 Beers, T. C., & Christlieb, N. 2005, *ARA&A*, 43, 531
 Boss, A. P., & Bodenheimer, P. 1979, *ApJ*, 234, 289
 Bromm, V., Coppi, P. S., & Larson, R. B. 2002, *ApJ*, 564, 23
 Bromm, V., & Larson, R. B. 2004, *ARA&A*, 42, 79
 Bromm, V., & Loeb, A. 2004, *New Astronomy*, 9, 353
 Bromm, V., Yoshida, N., Hernquist, L., & McKee, C. F. 2009, *Nature*, 459, 49
 Burkert, A., & Bodenheimer, P. 1993, *MNRAS*, 264, 798
 Clark, P. C., Glover, S. C. O., & Klessen, R. S. 2008, *ApJ*, 672, 757
 Clark, P. C., Glover, S. C. O., Klessen, R. S., & Bromm, V. 2011, *ApJ*, 727, 110
 Federrath, C., Banerjee, R., Clark, P. C., & Klessen, R. S. 2010, *ApJ*, 713, 269
 Freese, K., Bodenheimer, P., Spolyar, D., & Gondolo, P. 2008, *ApJ*, 685, L101
 Glover, S. C. O., & Abel, T. 2008, *MNRAS*, 388, 1627
 Haiman, Z., Thoul, A. A., & Loeb, A. 1996, *ApJ*, 464, 523
 Heger, A., & Woosley, S. E. 2002, *ApJ*, 567, 532
 Hosokawa, T., & Omukai, K. 2009, *ApJ*, 691, 823
 Iocco, F., Bressan, A., Ripamonti, E., Schneider, R., Ferrara, A., & Marigo, P. 2008, *MNRAS*, 390, 1655
 Iwamoto, N., Umeda, H., Tominaga, N., Nomoto, K., & Maeda, K. 2005, *Science*, 309, 451
 Jappsen, A.-K., Klessen, R. S., Larson, R. B., Li, Y., & Mac Low, M.-M. 2005, *A&A*, 435, 611
 Kitsionas, S., & Whitworth, A. P. 2002, *MNRAS*, 330, 129
 Klessen, R. S., & Burkert, A. 2000, *ApJS*, 128, 287
 Komatsu, E., et al. 2009, *ApJS*, 180, 330
 Krumholz, M. R., Klein, R. I., McKee, C. F., Offner, S. S. R., & Cunningham, A. J. 2009, *Science*, 323, 754
 Krumholz, M. R., McKee, C. F., & Klein, R. I. 2004, *ApJ*, 611, 399
 Mac Low, M.-M., & Klessen, R. S. 2004, *Reviews of Modern Physics*, 76, 125
 Machacek, M. E., Bryan, G. L., & Abel, T. 2001, *ApJ*, 548, 509
 Mayer, M., & Duschl, W. J. 2005, *MNRAS*, 358, 614
 McGreer, I. D., & Bryan, G. L. 2008, *ApJ*, 685, 8
 McKee, C. F., & Ostriker, E. C. 2007, *ARA&A*, 45, 565
 McKee, C. F., & Tan, J. C. 2008, *ApJ*, 681, 771
 Monaghan, J. J. 2005, *Reports of Progress in Physics*, 68, 1703
 Neufeld, D. A., & Kaufman, M. J. 1993, *ApJ*, 418, 263
 O’Shea, B. W., & Norman, M. L. 2007, *ApJ*, 654, 66
 Peters, T., Banerjee, R., Klessen, R. S., Mac Low, M., Galván-Madrid, R., & Keto, E. R. 2010, *ApJ*, 711, 1017
 Ripamonti, E. 2007, *MNRAS*, 376, 709
 Ripamonti, E., & Abel, T. 2004, *MNRAS*, 348, 1019
 Smith, R. J., Glover, S. C. O., Clark, P. C., Greif, T. H., & Klessen, R. S. 2011, *MNRAS*, submitted
 Springel, V. 2005, *MNRAS*, 364, 1105
 —. 2010a, *MNRAS*, 401, 791
 —. 2010b, *ARA&A*, 48, 391
 Stacy, A., Bromm, V., & Loeb, A. 2010a, *MNRAS*, accepted (arXiv:1010.0997)
 Stacy, A., Greif, T. H., & Bromm, V. 2010b, *MNRAS*, 403, 45
 Stahler, S. W., Palla, F., & Salpeter, E. E. 1986, *ApJ*, 302, 590
 Tan, J. C., & McKee, C. F. 2004, *ApJ*, 603, 383
 Tegmark, M., Silk, J., Rees, M. J., Blanchard, A., Abel, T., & Palla, F. 1997, *ApJ*, 474, 1
 Truelove, J. K., Klein, R. I., McKee, C. F., Holliman, II, J. H., Howell, L. H., Greenough, J. A., & Woods, D. T. 1998, *ApJ*, 495, 821
 Turk, M. J., Abel, T., & O’Shea, B. 2009, *Science*, 325, 601
 Turk, M. J., Clark, P., Glover, S. C. O., Greif, T. H., Abel, T., Klessen, R., & Bromm, V. 2011, *ApJ*, 726, 55
 Umeda, H., & Nomoto, K. 2002, *ApJ*, 565, 385
 Yoshida, N., Abel, T., Hernquist, L., & Sugiyama, N. 2003, *ApJ*, 592, 645
 Yoshida, N., Omukai, K., & Hernquist, L. 2008, *Science*, 321, 669
 Yoshida, N., Omukai, K., Hernquist, L., & Abel, T. 2006, *ApJ*, 652, 6
 Zinnecker, H., & Yorke, H. W. 2007, *ARA&A*, 45, 481